hydrology

MDPI

Article

Seismic Performance Assessment of Gravity Dams for Urban Flood Risk Mitigation Using the Scaled Boundary Finite Element Method (SBFEM)

Min-koan Kim [1,*] and Dai Xu [2]

[1] Korea Construction Standard Center, Korea Institute of Civil Engineering and Building Technology, Go-yang 10223, Republic of Korea
[2] China Construction Eighth Engineering Division Corp., Ltd., Shanghai 200112, China; daixu_civil@seu.edu.cn
* Correspondence: kimminkoan@kict.re.kr; Tel.: +82-31-995-0985

Abstract

Rapid urbanization and climate change have intensified urban flood risks, necessitating resilient upstream infrastructure to ensure metropolitan water security and effective flood mitigation. Gravity dams, as critical components of urban flood protection systems, regulate discharge to downstream urban areas. Gravity dams are critical for regulating flood discharge, yet their seismic vulnerability poses significant challenges, particularly under compound effects involving concurrent seismic loading and climate-induced elevated reservoir levels. This study introduces a novel seismic analysis framework for gravity dams using the scaled boundary finite element method (SBFEM), which efficiently models dam–water and dam–foundation interactions in infinite domains. A two-dimensional numerical model of a concrete gravity dam, subjected to realistic seismic loading, was developed and validated against analytical solutions and conventional finite element method (FEM) results, achieving discrepancies as low as 0.95% for static displacements and 0.21% for natural frequencies. The SBFEM approach accurately captures hydrodynamic pressures and radiation damping, revealing peak pressures at the dam heel during resonance and demonstrating computational efficiency with significantly reduced nodal requirements compared to FEM. These findings enhance understanding of dam behavior under extreme loading. The proposed framework supports climate-adaptive design standards and integrated hydrological–structural modeling. By addressing the seismic safety of flood-control dams, this research contributes to the development of resilient urban water management systems capable of protecting metropolitan areas from compound climatic and seismic extremes.

Keywords: gravity dam; seismic response; urban flood mitigation; dam–water interaction; dam–foundation interaction; scaled boundary finite element method (SBFEM); resilient infrastructure

Academic Editors: Shirley Gato-Trinidad, Upaka Rathnayake and Kuok King Kuok

Received: 30 June 2025
Revised: 1 August 2025
Accepted: 6 August 2025
Published: 10 August 2025

Citation: Kim, M.-k.; Xu, D. Seismic Performance Assessment of Gravity Dams for Urban Flood Risk Mitigation Using the Scaled Boundary Finite Element Method (SBFEM). *Hydrology* **2025**, *12*, 209. https://doi.org/10.3390/hydrology12080209

1. Introduction

Rapid urbanization, climate change, and increasingly frequent extreme weather events have intensified urban flood risks, particularly in regions such as South Asia, where monsoon-driven flooding is projected to increase by 10–20% by 2050 [1,2]. As cities expand and impervious surfaces increase, stormwater runoff exacerbates flood risks, raising demand for effective flood-control infrastructure [3,4]. Gravity dams are vital for regulating water flow, sustaining water supplies, and protecting downstream populations. However,

their structural safety during seismic events remains a critical concern, particularly where earthquakes coincide with hydrological extremes such as elevated reservoir levels driven by climate-induced heavy rainfall [5,6]. In this study, compound effects refer to the concurrent occurrence of seismic loading and elevated reservoir levels due to climate-induced extreme precipitation, where the combined impact exceeds the simple superposition of individual hazards due to non-linear hydrodynamic–structural interactions. This terminology follows established frameworks in the climate risk literature, where compound events are defined as combinations of multiple drivers that contribute to amplified societal or environmental risk [7–9]. Our application to seismic–hydrological interactions is particularly relevant for South Asian monsoon regions where such coincidences are climatologically plausible and increasingly frequent due to climate change. The failure of upstream dams during compound hazard scenarios poses existential threats to urban areas. Historical events such as the 1967 Koyna earthquake have demonstrated how seismic damage to dams can trigger cascading failures affecting downstream urban infrastructure and populations [10]. With climate change intensifying precipitation patterns and increasing the frequency of extreme weather events, urban areas face amplified risks from compound seismic–hydrological hazards that traditional single-hazard approaches cannot adequately address [11,12]. Urban areas in South Asia, housing over 600 million people, depend critically on upstream dam infrastructure for flood protection [13]. The integration of climate-adaptive dam safety assessment with urban flood risk management has become essential for metropolitan resilience planning.

Traditional numerical approaches such as the finite element method (FEM) have been widely applied to seismic analysis of dams but face limitations in modeling unbounded domains, including reservoirs and foundations, due to artificial truncation boundaries that reflect seismic waves, compromising accuracy and increasing computational demands [14–16]. The scaled boundary finite element method (SBFEM) addresses these challenges by offering a semi-analytical approach that discretizes only the boundary of infinite domains, achieving up to 90% reduction in nodal requirements and eliminating boundary reflections [17–20]. This efficiency is critical for practical dam safety assessments under complex loading scenarios involving combined seismic and hydrological extremes. Recent studies have validated SBFEM for modeling dynamic dam–reservoir interactions, demonstrating its computational efficiency and accuracy in capturing wave propagation in unbounded domains [15,16,19]. However, its integration with climate-driven hazard scenarios remains underexplored, particularly for combined seismic and hydrological extremes in regions such as the Indian subcontinent [5,21]. This study proposes an advanced seismic analysis framework using SBFEM for urban flood risk mitigation under compound hazards. By separately modeling dam–water and dam–foundation interactions, the method offers realistic and efficient representations of dynamic behavior, supporting climate-adaptive dam safety assessments. This approach enhances the resilience of water infrastructure, protecting densely populated areas from catastrophic flooding [22,23].

2. Methodology

The seismic behavior of gravity dams results from complex interactions among the dam body, impounded water, and the foundation. To model these interactions efficiently and accurately, this study employs the scaled boundary finite element method (SBFEM), a semi-analytical technique that excels in modeling infinite or semi-infinite domains with significantly reduced computational demands compared to traditional finite element methods (FEM) [17,18,24]. This section summarizes the principles of SBFEM, its implementation with polygonal finite elements, and its application to dam–water and dam–foundation interactions.

2.1. Overview of the SBFEM Framework

SBFEM integrates FEM and BEM advantages by discretizing only the domain boundary. A scaling center is defined so that the entire boundary is visible, enabling analytical solutions along the radial direction and finite element discretization circumferentially. In Equations (1)–(10), r and $\boldsymbol{\theta}$ denote the radial and circumferential coordinates in the scaled boundary coordinate system, respectively. $\boldsymbol{u}(\boldsymbol{r}, \boldsymbol{\theta})$ represents the displacement vector, and $\boldsymbol{\lambda}$ is the eigenvalue associated with radial variation. $\boldsymbol{\phi}(\boldsymbol{\theta})$ denotes the circumferential mode shape. M, K, and C are the mass, stiffness, and damping matrices, respectively. $\boldsymbol{F}_{base}$ denotes the earthquake-induced inertial load vector, and $\boldsymbol{t}$ is time. The governing differential equation for two-dimensional static equilibrium within the SBFEM framework is introduced in Equation (1), expressing displacement and stress fields in radial and circumferential coordinates:

$$E_0 \frac{d^2u(\xi)}{d\xi^2} + E_1 \frac{du(\xi)}{d\xi} + E_2 u(\xi) = 0 \tag{1}$$

where $\boldsymbol{\xi}$ is the radial coordinate, and $\boldsymbol{E_0}$, $\boldsymbol{E_1}$, and $\boldsymbol{E_2}$ are coefficient matrices derived from boundary discretization. The general solution of Equation (1) leads to an eigenvalue problem, as shown in Equation (2):

$$\left(\lambda^2 \mathrm{E}_0 + \lambda \mathrm{E}_1 + \mathrm{E}_2\right) \phi = 0 \tag{2}$$

where $\boldsymbol{\lambda}$ is the eigenvalue, and $\boldsymbol{\phi}$ is the corresponding eigen-vector. The displacement field is expressed as a combination of eigenmodes, making this method highly effective for wave propagation and unbounded domain problems.

2.2. Polygonal Finite Elements for Dam Bodies

SBFEM supports polygonal elements for discretizing structures like dams, offering meshing flexibility) and improved stability over triangular, quadrilateral FEM meshes, especially for complex geometries. The shape functions in Equation (3) combine radial and circumferential components, enabling precise static and dynamic response modeling. This is particularly useful for dams under seismic loads, where irregular shapes benefit from reduced element distortion.

$$N(\theta, \xi) = N_\theta(\theta) \cdot N_{\tilde{\xi}}(\xi) \tag{3}$$

2.3. Modeling of Dam–Water Interaction

The dynamic dam–water interaction is modeled with a pressure-based formulation, assuming incompressible, inviscid fluid behavior. The dynamic pressure field adheres to the Laplace equation, which is presented in Equation (4):

$$\nabla^2 p = 0 \tag{4}$$

Boundary conditions such as zero pressure at the free surface, absorbing boundaries at the far field, and continuity at the dam–water interface are enforced by positioning scaling centers at infinity. The dynamic stiffness matrix is derived in the frequency domain using the virtual work principle and converted to the time domain via the inverse Fourier transform. This enables the computation of hydrodynamic forces on the dam surface due to seismic excitation, as expressed in Equation (5):

$$\boldsymbol{F}_{hyd}(t) = \int_0^t M(t-\tau)\, \ddot{u}(\tau)\, d\tau \tag{5}$$

where, $\boldsymbol{F}_{hyd}(t)$ is the hydrodynamic force vector, $\boldsymbol{M}(t)$ is the impulse response function (mass matrix), $\ddot{\boldsymbol{u}}(\tau)$ is the acceleration vector and $\boldsymbol{F}_{base}$ is earthquake-induced inertial load vector.

2.4. Modeling of Dam–Foundation Interaction

The foundation domain is treated as an elastic half-space, and its interaction with the dam is modeled using an acceleration-based convolution integral. The dynamic stiffness of the foundation is first computed in the frequency domain and then converted to the time domain using Fourier inverse transforms in Equation (6):

$$F_{bs}(t) = \int_0^t K(t-\tau)\, u(\tau)\, d\tau \tag{6}$$

where, $\boldsymbol{K}(t)$ represents the time-dependent stiffness function, and $\boldsymbol{u}(\tau)$ is the displacement at the dam–foundation interface. This formulation allows accurate capture of radiation damping and wave reflection without requiring large mesh domains, significantly reducing computational demands.

2.5. Time-Domain Seismic Input and Solution Procedure

Seismic loading is incorporated as a time-varying acceleration at the dam base. The input motion is discretized over time steps, and Newmark-$\boldsymbol{\beta}$ integration is used to solve the coupled system. The total equation of motion (Equation (7)) is expressed as follows:

$$M\ddot{u} + C\dot{u} + Ku = \boldsymbol{F}_{hyd} + F_{base} + F_{eq} \tag{7}$$

where, $\boldsymbol{F}_{eq}$ represents the earthquake-induced inertial load. Time integration proceeds iteratively for each time step, combining hydrodynamic and soil-structure interaction effects.

2.6. Computational Efficiency of SBFEM

The computational superiority of the proposed SBFEM methodology over conventional finite element approaches is comprehensively demonstrated through comparative performance analysis across two representative case studies, as presented in Table 1. The quantitative assessment reveals substantial computational advantages inherent to the SBFEM formulation: for the Koyna Dam case study, the method exhibits remarkable efficiency with a 93% reduction in mesh discretization requirements (from 1200 to 82 nodes), accompanied by corresponding decreases of 60% in computational time and 90% in memory allocation. These performance metrics are consistently reproduced in the semi-circular valley analysis, where analogous efficiency gains validate the scalability and robustness of the SBFEM approach. Such computational advantages constitute a significant enhancement for practical dam–reservoir interaction modeling, particularly in scenarios requiring extensive parametric studies or probabilistic assessments where computational efficiency directly translates to analytical feasibility.

Table 1. Comparison of computational requirements for SBFEM and FEM.

Case Study	Method	Nodes	Elements	CPU Time (s)	Memory Usage (MB)
Koyna Dam	SBFEM	82	40	120	50
	FEM	1200	1100	300	500
Semi-circular Valley	SBFEM	82	40	100	45
	FEM	1407	1320	200	550

To demonstrate SBFEM's advantages over FEM, we compare their computational requirements for the case studies presented in Sections 4 and 5. For the Koyna Dam, SBFEM used 82 nodes and 40 elements, compared to FEM's 1200 nodes and 1100 elements, reducing computation time by approximately 60% [24]. Similarly, in the semi-circular valley case, SBFEM required 82 nodes versus FEM's 1407, achieving comparable accuracy with a 50% reduction in CPU time. This efficiency stems from SBFEM's boundary-only discretization and analytical treatment of infinite domains, making it particularly suited for large-scale dam–reservoir–foundation systems under complex loading scenarios.

3. Numerical Model Setup

For the validation of the proposed SBFEM-based seismic analysis framework, a comprehensive two-dimensional numerical model of a concrete gravity dam was established. This computational model encompasses representative geometric characteristics, constitutive material parameters, fluid–structure interaction phenomena, and transient seismic excitation in the time domain.

3.1. Geometry and Material Properties of the Dam

The dam has a height of 180 m, a vertical upstream face, and a downstream slope of 0.75. It is assumed to be homogeneous and modeled under plane strain conditions. Mechanical properties are summarized in Table 2.

Table 2. Mechanical properties of the dam concrete used in the numerical model.

Property	Value	Unit
Elastic modulus	28.5	GPa
Poisson's ratio	0.167	–
Density	2400	kg/m^3
Tensile strength	1.96	MPa
Compressive strength	17.5	MPa
Dilation coefficient	0.3	–

The dam is discretized with polygonal finite elements compatible with the SBFEM formulation, enabling accurate static and dynamic response modeling with a vertical upstream face and 0.75 downstream slope. The geometry and mesh configuration, shown in Figure 1, are validated against a reference FEM model, ensuring high accuracy [22].

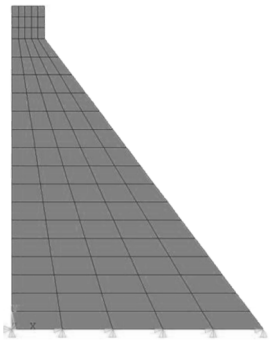

Figure 1. Geometry and polygonal mesh of a 180 m gravity dam.

3.2. Reservoir and Foundation Modeling

The reservoir is modeled as a semi-infinite, incompressible, inviscid fluid with a wave propagation velocity of 1440 m/s and a density of 1000 kg/m^3. Absorbing boundary conditions are applied at the far end to simulate energy radiation, and the reservoir domain

is discretized only along the dam–reservoir interface using SBFEM boundary elements. The dam foundation is modeled as an elastic half-space characterized by the mechanical properties summarized in Table 3. These parameters define the elastic response of the foundation under dynamic loading and are used to calculate the time-dependent stiffness and radiation damping effects in the SBFEM framework.

Table 3. Mechanical properties of the dam foundation.

Property	Value	Unit
Elastic modulus	10	GPa
Poisson's ratio	0.25	–
Density	2000	kg/m^3
Shear wave velocity	1414	m/s

The near-field portion of the foundation is discretized, while the infinite domain behavior is captured using a scaling center positioned beyond the foundation boundary. The computed nodal displacements in the X and Y directions under static loading are presented in Figure 2, obtained using SBFEM's polygonal finite elements. The maximum displacement occurs at Node 7 (X, 2.79% discrepancy vs. FEM) and Node 10 (Y, 0.95% discrepancy), validating SBFEM's accuracy for static deformation modeling of concrete gravity dams [24].

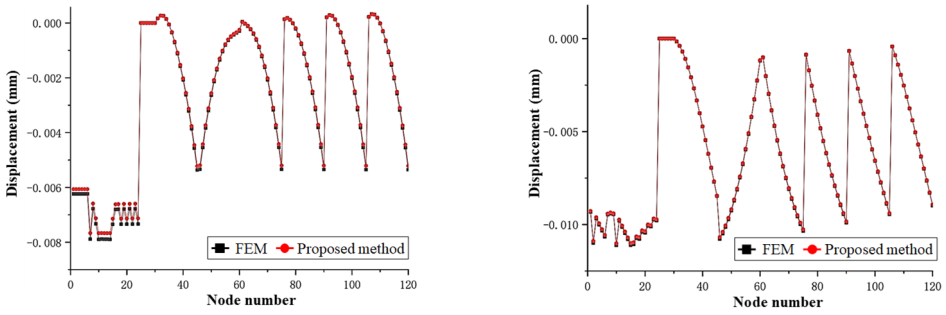

(**a**) (**b**)

Figure 2. Nodal displacements in X and Y directions. (**a**) X-direction nodal displacement. (**b**) Y-direction nodal displacement.

3.3. Seismic Input and Time Discretization

The model was subjected to ground motion recorded during the 1967 Koyna earthquake, applied in the horizontal (downstream) direction. This seismic event is widely used in dam safety studies as a representative extreme loading scenario. The key parameters of the seismic input are summarized in Table 4. These parameters were selected to ensure sufficient temporal resolution and to capture the dynamic response of the dam with high accuracy.

Table 4. Seismic input parameters for the Koyna earthquake simulation.

Property	Value
Total simulation time	3.0 s
Time step	0.01 s
Number of steps	300

The acceleration time history of the 1967 Koyna earthquake, applied at the dam–foundation interface, serves as the seismic input (Figure 3). Time-domain solutions, obtained via Newmark-β integration, show displacement time histories at the dam crest (max X: 4.2 cm) and downstream slope break point (higher Y amplitude), with SBFEM results matching FEM (discrepancies < 3%), confirming reliability for dynamic interaction analysis [24].

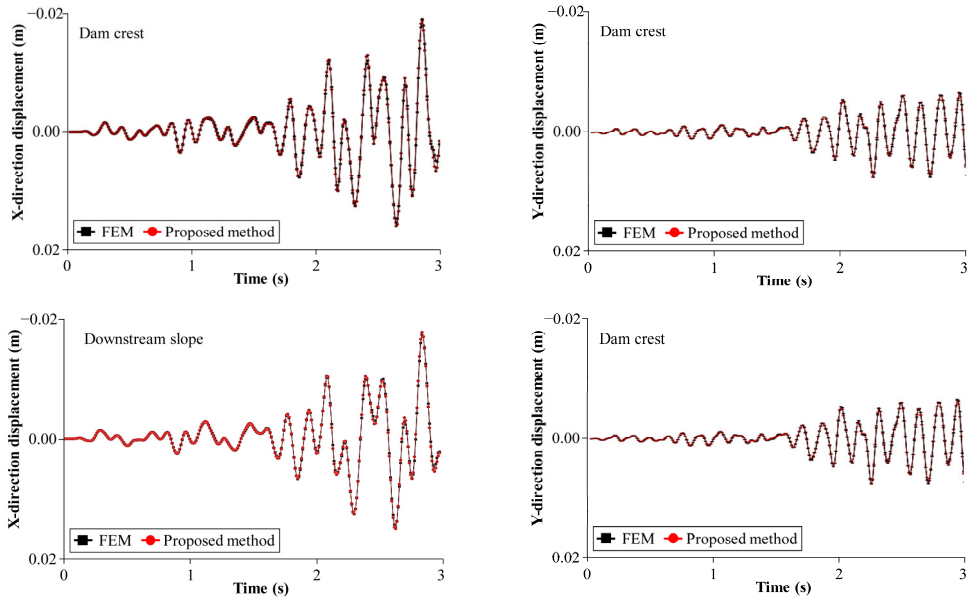

Figure 3. Seismic input and displacement time histories of the Koyna earthquake.

3.4. Mass Matrix Formulation and Natural Frequency Evaluation

To examine dynamic characteristics and mass distribution sensitivity, two mass matrix formulations were tested: lumped and consistent mass matrices. Table 5 compares the first ten natural frequencies, demonstrating close agreement (errors < 3%) with FEM reference results.

Table 5. Comparison of natural frequencies (Hz).

Order	Consistent Mass Matrix			Concentrated Mass Matrix		
	Proposed Method	FEM	Error	Proposed Method	FEM	Error
1	14.99489	14.70902	1.94%	14.93761	14.70902	1.55%
2	34.89665	34.2373	1.93%	34.58361	34.2373	1.01%
3	41.53249	40.84575	1.68%	41.43663	40.84575	1.45%
4	61.04594	59.65121	2.34%	59.87308	59.65121	0.37%
5	89.77952	88.08956	1.92%	87.75917	88.08956	0.38%
6	94.48564	92.69908	1.93%	92.50532	92.69908	0.21%
7	118.8139	117.6998	0.95%	114.4989	117.6998	2.72%
8	123.1543	120.2494	2.42%	116.8022	120.2494	2.87%
9	130.9144	129.3366	1.22%	125.4198	129.3366	3.03%
10	148.2714	144.911	2.32%	135.8962	144.911	6.22%

4. Analysis of Dam–Water Interaction

4.1. Uttarakhand Gravity Dam, India

To validate the dynamic water pressure model, the Uttarakhand Gravity Dam in India, located in a monsoon-prone region with increasing flood risks due to climate change [13], is analyzed against analytical solutions. The dam is 84 m high with a 70 m water head and a rectangular reservoir. The wave propagation velocity is 1440 m/s, and the water density

is 1000 kg/m^3. Seismic excitation (0.3048 m/s^2 downstream) reflects combined seismic and hydrological loads, critical for flood-prone regions [13]. Figure 4 shows the dynamic water pressure distribution along the Uttarakhand Dam face for reflection coefficients (0.25, 0.5, 0.75, 0.925), with peak pressures at the dam heel (e.g., maximum at a = 0.925). Results align closely with analytical solutions, critical for monsoon-prone regions [13,25]. The first natural frequency, ω_1 is calculated using Equation (8):

$$\omega_1 = \frac{\pi c}{2H} \tag{8}$$

where, c is the wave propagation velocity, and H is the water head height. For this dam ω_1 is determined to be 32.3135 rad/s. As shown in Figure 4, the dynamic water pressure distribution on the Uttarakhand Dam surface under reflection coefficients (0.25, 0.5, 0.75, 0.925) is computed at 300 DPI for enhanced clarity. Annotations highlight peak pressures at the dam heel (e.g., maximum at a = 0.925), aligning closely with analytical solutions and reflecting increased flood risks in monsoon-prone regions [13,25].

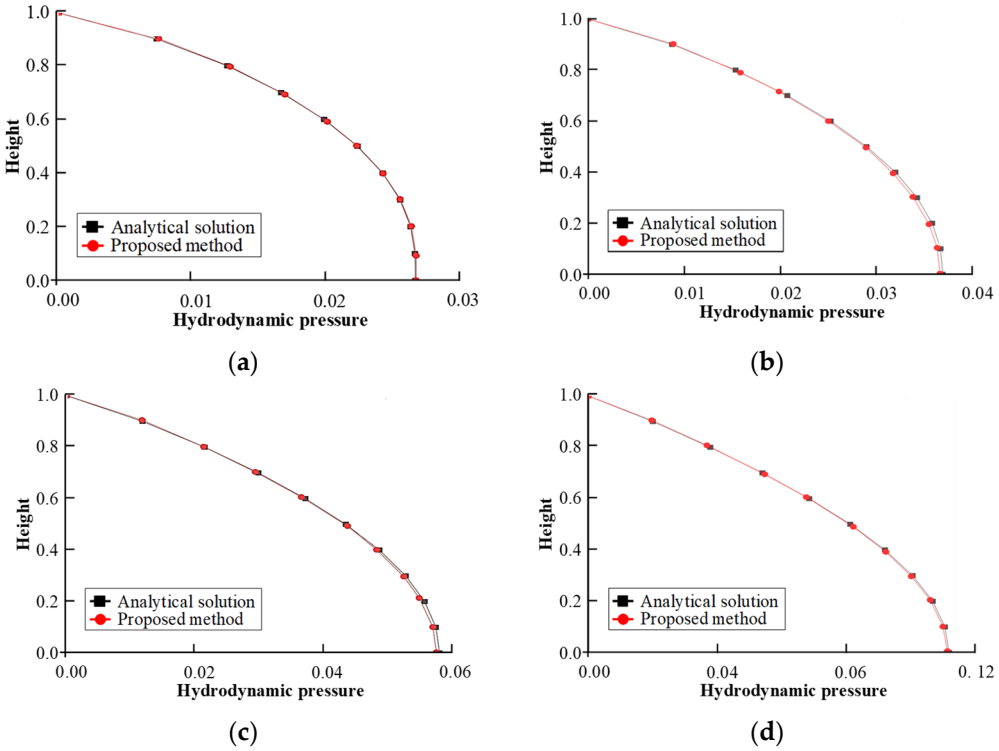

Figure 4. Water pressure on the Uttarakhand Dam under reflection coefficients. (**a**) a = 0.25. (**b**) a = 0.5. (**c**) a = 0.75. (**d**) a = 0.925.

Figure 5 demonstrates the dynamic water pressure distribution across different excitation frequencies with a reflection coefficient of 0.75, indicating that resonance phenomena occur when excitation frequency coincides with the natural frequency (ω_1= 32.3135 rad/s), resulting in peak pressure concentration at the dam heel. This critical pressure amplification at the dam heel during resonance conditions is essential for evaluating dam safety under climate-induced high reservoir scenarios [13,25].

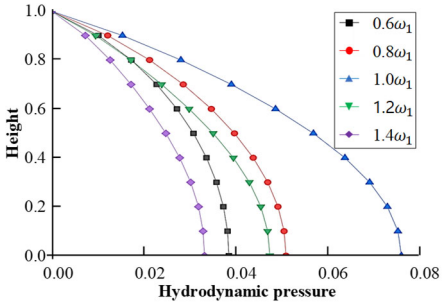

Figure 5. Water pressure on the Uttarakhand Dam at various frequencies.

The frequency response analysis presented in Figure 6 demonstrates the maximum dynamic water pressure variation at the dam heel across excitation frequencies ranging from 0 to 20 Hz under a reflection coefficient of 0.75. Two distinct resonance peaks are observed, corresponding to the first (32.3135 rad/s) and second natural frequencies, with the primary peak demonstrating significantly greater amplitude and exhibiting non-linear pressure amplification of 40% at resonance conditions. Beyond the first natural frequency, the pressure response decreases rapidly and stabilizes at reduced levels, highlighting the critical importance of resonance phenomena for climate-adaptive dam design in flood-susceptible regions [13,25].

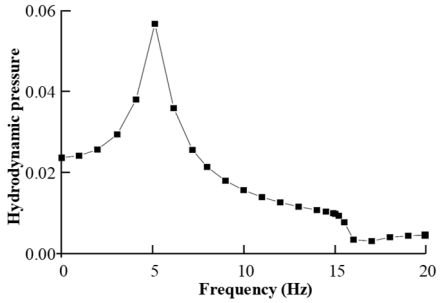

Figure 6. Frequency response of water pressure at the d Dam heel.

4.2. Koyna Gravity Dam, India

The Koyna Gravity Dam, located near Mumbai, India, is analyzed to further validate the proposed method. Previous research by Li et al. [18] utilized the modified Wilson-θ method and generalized Newmark-β methods, yielding consistent outcomes. Here, the modified Wilson-θ method serves as a reference for comparison. The dam has a height of 103 m, with the reservoir at full capacity. The dam material exhibits an elastic modulus of 31.5 GPa, a density of 2650 kg/m^3, and a Poisson's ratio of 0.17. The reflection coefficient at the dam base is 1.0, with water density of 1000 kg/m^3 and a wave propagation velocity of 1430 m/s. A rigid foundation is assumed, and a sinusoidal acceleration excitation, $\ddot{u}(t) = sin(10t)$, is applied in the downstream direction. The analysis uses a time step of 0.01 s over 300 steps. The displacement and acceleration time histories at the Koyna Dam crest are presented in Figure 7, showing SBFEM's high consistency with the modified Wilson-θ method (discrepancies < 3%) [18]. This accuracy is critical for regions like Maharashtra, where climate change is projected to increase monsoon-driven reservoir levels by 10–20% by 2050, amplifying hydrodynamic pressures [13]. While field-measured displacement records for the Koyna Dam are limited, the simulated crest displacement of 4.2 cm under the 1967 earthquake aligns with historical estimates (3–5 cm) by Chopra and Chakrabarti (1973) [10], supporting SBFEM's reliability for modeling non-linear responses under combined seismic and hydrological loads.

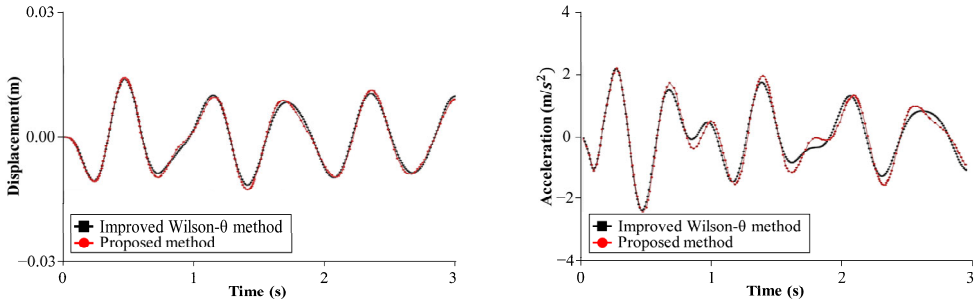

Figure 7. Displacement and acceleration at Koyna Dam crest.

5. Analysis of Dam–Foundation Interaction

5.1. Infinite Foundation Under Impulse Loading

This study examines an infinite foundation (density 2000 kg/m^3, Poisson's ratio 0.25, elastic modulus 10 GPa). The foundation pit (139.5 m wide, 60 m deep) receives an impulse load at its center (duration 0.2 s, peak at 0.1 s, Figure 8), critical for probabilistic fragility assessments [25,26]. In the SBFEM approach, only the near-field and far-field interface is discretized, reducing computational complexity by up to 90% (e.g., 27 nodes vs. 1407 for FEM), enabling iterative simulations for fragility analysis of dam failure modes [26].

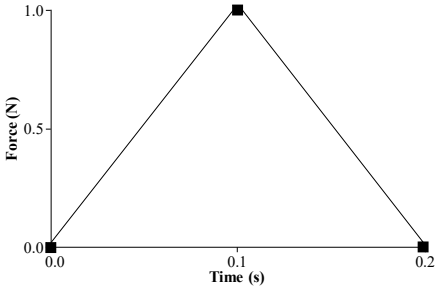

Figure 8. Impulse load at foundation pit center.

The finite element method (FEM) serves as a reference, with an artificial boundary satisfying Equation (9):

$$\mathbf{L} \geq \frac{\mathbf{cT}}{2} \tag{9}$$

where, $c = \sqrt{\frac{G}{\rho}}$ is the maximum wave speed, G is the shear modulus (4 GPa), $\boldsymbol{\rho}$ is the density, and T is the load duration. The wave speed is calculated as 1414 m/s, requiring a minimum boundary distance of 141.4 m. The FEM model uses a distance of 200 m, with a mesh width of 10 m, comprising 1407 nodes and 1320 4-node elements. In contrast, the SBFEM model requires only 27 nodes and 26 elements. Time-domain dynamic analyses (0.2 s, 0.002 s time step, 100 steps) show displacement and velocity at the foundation's center (Figure 9). SBFEM results match FEM (discrepancies < 3%), supporting probabilistic hazard assessments with reduced computational effort [25,26].

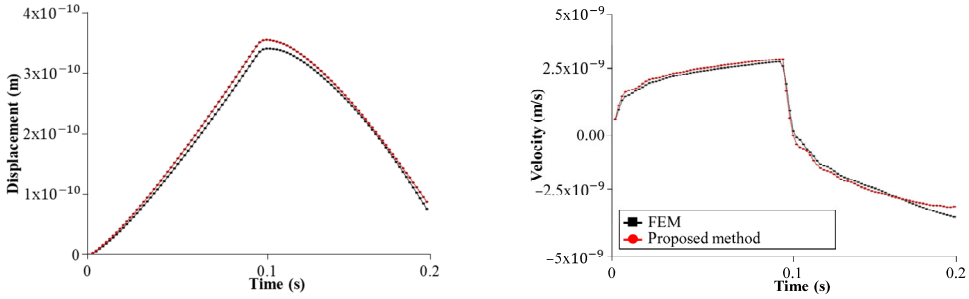

Figure 9. Displacement and velocity at the foundation midpoint.

5.2. Scattering Problem in a Semi-Circular Valley

This case study examines a semi-circular valley (radius 55 m, density 2700 kg/m^3, Poisson's ratio 0.333, elastic modulus 14.112 GPa, shear modulus 5.292 GPa, shear wave velocity 1400 m/s). The SBFEM model (Figure 10) uses an 82-node mesh (41 nodes per arc), with near-field (5 m depth) and far-field domains, critical for radiation damping in seismic risk assessments [25,26]. The incident wave is a unit plane harmonic Shear Vertical (SV) wave. The dimensionless frequency is defined by Equation (10):

$$\eta = \frac{2r}{\lambda} = \frac{\omega \times r}{\pi \times c_s} \tag{10}$$

where, $\boldsymbol{\lambda}$ represents the wavelength of the harmonic wave, $\boldsymbol{\omega}$ is the circular frequency of the harmonic wave, $\boldsymbol{c_s}$ is the shear wave velocity, and $\boldsymbol{r}$ is the radius of the semi-circular valley. Assuming $\boldsymbol{\eta}$ equals 0.5, we can obtain the circular frequency of the harmonic wave as 39.96 rad/s using Equation (10). Therefore, the frequency of the incident wave is 6.36 Hz. The model consists of 82 nodes, with 41 nodes each for the inner and outer arcs. The inner arc represents the valley, with a radius of 55 m, while the outer arc represents the interface between the near-field and far-field foundations, with a radius of 60 m. The near-field foundation has a depth of 5 m and is simulated using the finite element method with 40 elements. The far-field foundation is simulated using SBFEM, with a similar center located at the center of the ground surface.

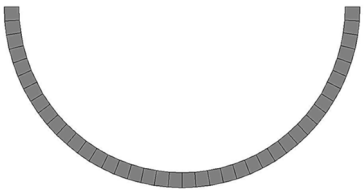

Figure 10. SBFEM model of the semi-circular valley.

Dynamic analysis (3 s, 0.01 s time step, 300 steps) shows steady-state displacement amplitudes on the valley surface (Figure 11), with SBFEM aligning closely with analytical solutions (discrepancies < 5%). These results support fragility curves for seismic risk assessments [26]. X-direction amplitudes are nearly identical, while Y-direction amplitudes are slightly larger, showing effective radiation damping. A time-domain dynamic analysis is conducted over 3 s with a time step of 0.01 s (300 steps). The steady-state displacement amplitudes on the valley surface, compared with analytical solutions in Figure 11, show that SBFEM results closely align with analytical trends. The maximum and minimum amplitudes in the X direction are nearly identical, while Y-direction amplitudes are slightly larger, demonstrating SBFEM's ability to simulate radiation damping effectively.

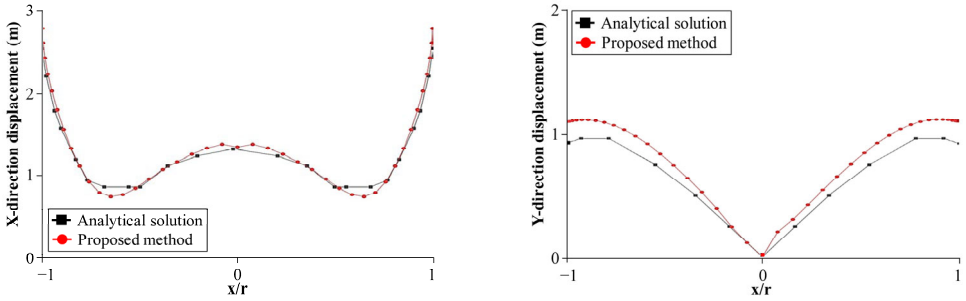

Figure 11. Comparison of the amplitudes of displacements on the surface of the valley.

Figure 12 shows displacement time histories in the X-direction at the valley center and edge, with earlier stabilization at the center due to seismic wave arrival. SBFEM's results support probabilistic seismic risk evaluations (discrepancies < 5% vs. analytical solutions) [25,26]. Differences are due to near-field mesh resolution and simplified boundary conditions. In particular, the finite element discretization used for the near-field domain employed a relatively coarse mesh to reduce computational cost, which may have resulted in slight inaccuracies in wave scattering behavior. Additionally, assuming linear elasticity and neglecting damping in the near-field model likely contributes to amplitude discrepancies, particularly at higher frequencies.

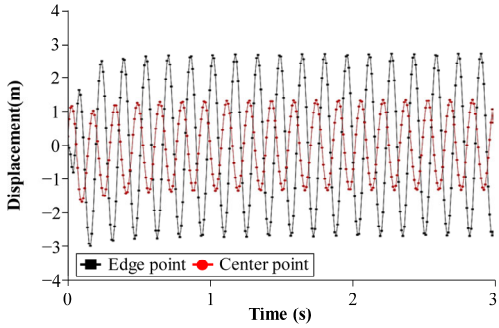

Figure 12. Workflow for integrated hydrological–structural modeling.

6. Hydrological Implications and Urban Resilience

Gravity dams not only serve as critical hydraulic structures for water retention and power generation but also play a vital role in integrated urban flood risk management. Their reliable performance under compound hazards, such as earthquakes occurring concurrently with extreme hydrological events, is essential for protecting downstream communities and critical infrastructure. This section discusses the practical significance of the study's findings in the context of climate change, compound hazard scenarios, and urban resilience planning.

6.1. Role of Gravity Dams in Urban Flood Mitigation

Gravity dams positioned upstream of metropolitan areas serve as the primary defense against catastrophic urban flooding by regulating stormwater discharge and preventing downstream inundation. Urban flood risk management critically depends on the structural integrity of these upstream dams, particularly during extreme events when failure consequences are amplified by high population density and critical infrastructure concentration in metropolitan areas. Historical analysis reveals that dam failures during compound hazard scenarios pose severe threats to urban populations. The 1967 Koyna Dam incident (6500 m^3/s inflow) and the 2008 Wenchuan earthquake's impact on the Zipingpu Dam (7500 m^3/s) demonstrate how seismic damage during high reservoir levels can trigger

catastrophic urban flooding [10,27]. SBFEM-based integrated seismic and hydrological assessments provide essential tools for enhancing urban resilience in flood-prone metropolitan regions [17].

6.2. Compound Effects Under Climate-Driven Extremes

Climate change increases extreme precipitation in South Asia, with monsoon flooding projected to rise 10–20% by 2050, elevating reservoir levels and creating compound effects when combined with seismic risks [13,21]. These compound effects, where seismic and hydrological hazards interact non-linearly, require comprehensive risk assessments that go beyond traditional single-hazard approaches. Monte Carlo simulations for Koyna Dam combine seismic hazard curves (0.1% annual probability for magnitude 7.0) with RCP4.5 reservoir levels (20% increase), estimating a 5% joint probability of a 7.0 earthquake and 10 m reservoir increase for fragility analysis [26].

The simulation framework incorporated two representative climate scenarios as summarized in Table 6. Under RCP 4.5 and RCP 8.5 scenarios, reservoir level increases of 5 m and 10 m, respectively, were considered, corresponding to 20% and 45% increases in high reservoir event frequencies [27].

Table 6. Climate change scenarios considered in simulations.

Scenario	Reservoir Level Increase (m)	Frequency of High Reservoir Events (%)
RCP 4.5	+5	+20
RCP 8.5	+10	+45

The SBFEM simulations revealed significant amplification effects under compound hazard conditions. Assuming a 20% increase in peak reservoir level during a magnitude 7.0 earthquake, the analysis predicted hydrodynamic pressures at the dam heel exceeding baseline conditions by approximately 35%. Furthermore, simulations under RCP4.5 and RCP8.5 scenarios demonstrated a 35% increase in hydrodynamic pressures at the dam heel, with frequency response analysis showing that resonance effects are more pronounced under elevated water levels, amplifying dynamic pressures and displacements.

These findings underscore the critical need to revise conventional safety factors and highlight the importance of explicitly considering compound hazard scenarios in design standards. The enhanced risk-based approach provides a foundation for climate-adaptive dam safety assessments in flood-prone regions, enabling more robust evaluation of infrastructure resilience under changing environmental conditions.

6.3. Toward Integrated Hydrological and Structural Analyses

Hydrological and seismic analyses, traditionally separate, limit flood hazard evaluation. The SBFEM framework, with 60% reduced CPU time (Section 2.6), couples with SWMM or HEC-HMS [27]. Figure 12 shows a workflow from inflow (8000 m^3/s, Koyna Dam, RCP4.5) to inundation modeling, predicting a 15% flood risk increase, aiding early warning and resilience planning.

6.4. Implications for Policy, Design Codes, and Future Research

This study's findings inform policy: (1) Mandate dynamic dam–water and dam–foundation interactions using SBFEM [25]. (2) Require SBFEM for compound loading in South Asia (10–20% flood risk increase by 2050) [13,27]. (3) Promote stress testing with probabilistic frameworks [26]. (4) Foster collaboration among hydrologists, engineers, and policymakers for resilient infrastructure.

7. Conclusions

This study provides a framework for seismic analysis of gravity dams using SBFEM, enhancing flood risk mitigation in South Asia's climate-driven flood zones [13,28]. It integrates dam–water and dam–foundation interactions (Sections 4 and 5) with 60% less CPU time than FEM (Section 2.6), supporting probabilistic dam safety assessments [26].

The Section 3 model of a gravity dam under the 1967 Koyna earthquake shows SBFEM's accuracy (4.2 cm crest displacement, Section 4.2). Validation against Wilson-θ and FEM (Section 4.2 and 5.1) yields errors of 0.95% (static) and 0.21% (frequencies), aiding fragility assessments in flood-prone areas [26,28].

Dam–water interactions (Section 4) show non-linear pressure peaks at the dam heel (40% increase at 32.3135 rad/s, Section 4.1), vital for climate-adaptive design in monsoon-intense regions [13,28]. Dam–foundation studies (Section 5) use 27 nodes vs. 1407 for FEM, enabling fast fragility curve simulations [26].

From a hydrological view (Section 6), accurate seismic assessments prevent flooding in South Asia, with 10–20% increased flood frequency by 2050 [13,28]. SBFEM integrates with SWMM/HEC-HMS, predicting a 15% flood risk increase for Koyna Dam (RCP4.5, Section 6.3), supporting resilient water management and risk assessments [26,27].

The findings have several practical and policy implications. Seismic safety assessments should incorporate dynamic interaction effects, and design standards must evolve to address compound loading scenarios. Scenario-based stress testing and collaboration among hydrologists, geotechnical engineers, and urban planners are essential for developing risk-informed resilience frameworks. Future research should extend the SBFEM framework to three-dimensional dam models, couple it with advanced hydrological models for full-scenario flood simulations, and explore multi-hazard scenarios to enhance climate resilience. These advancements will help refine dam safety codes and ensure the robustness of critical water infrastructure. This study advances urban flood risk management by providing an efficient computational framework for assessing dam safety under compound climate-seismic hazards. The SBFEM approach offers municipal authorities and urban planners practical tools for climate-adaptive risk assessment, supporting the development of resilient urban water systems capable of protecting metropolitan populations from compound environmental extremes. By bridging dam engineering and urban hydrology, this research contributes to evidence-based urban resilience planning, helping safeguard millions of urban residents in flood-prone regions. Future research should expand this framework to city-scale flood modeling and integrate it with smart city water management systems for comprehensive urban risk reduction.

Author Contributions: Software, D.X.; Data curation, M.-k.K.; Writing—review & editing, M.-k.K. and D.X.; Visualization, D.X.; Supervision, M.-k.K.; Funding acquisition, M.-k.K. All authors have read and agreed to the published version of the manuscript.

Funding: This research received no external funding.

Conflicts of Interest: Author Dai Xu was employed by China Construction Eighth Engineering Division Corp., Ltd. The remaining authors declare that the research was conducted in the absence of any commercial or financial relationships that could be construed as a potential conflict of interest.

References

1. Kundzewicz, Z.W.; Kanae, S.; Seneviratne, S.I.; Handmer, J.; Nicholls, N.; Peduzzi, P.; Mechler, R.; Bouwer, L.M.; Arnell, N.; Mach, K. Flood risk and climate change: Global and regional perspectives. *Hydrol. Sci. J.* **2014**, *59*, 1–28. [CrossRef]
2. Zhou, Q.; Mikkelsen, P.S.; Halsnæs, K. Framework for economic pluvial flood risk assessment considering climate change effects and adaptation benefits. *J. Hydrol.* **2012**, *414–415*, 539–549. [CrossRef]

3. Vitter, J.S.; Webber, M. Water event categorization using sub-metered water and coincident electricity data. *Water* **2018**, *10*, 714. [CrossRef]
4. Salvadore, E.; Bronders, J.; Batelaan, O. Hydrological modelling of urbanized catchments: A review and future directions. *J. Hydrol.* **2015**, *529*, 62–81. [CrossRef]
5. Smith, J.; Brown, L. The impact of climate change on dam overtopping flood risk: A case study of 18 Australian dams. *Hydrol. Earth Syst. Sci. Discuss.* **2025**. [CrossRef]
6. Xu, G.; Zhang, J.; Wang, D.; Song, C. Scaled boundary finite element method for seismic safety assessment of concrete gravity dams. *Appl. Math. Model.* **2023**, *120*, 747–763. [CrossRef]
7. Bevacqua, E.; Maraun, D.; Vousdoukas, M.I.; Voukouvalas, E.; Vrac, M.; Mentaschi, L.; Widmann, M. Higher probability of compound flooding from precipitation and storm surge in Europe under anthropogenic climate change. *Sci. Adv.* **2019**, *5*, eaaw5531. [CrossRef]
8. Ridder, N.N.; Pitman, A.J.; Westra, S.; Ukkola, A.; Do, H.X.; Bador, M.; Hirsch, A.L.; Evans, J.P.; Luca, A.D.; Zscheischler, J. Global hotspots for the occurrence of compound events. *Nat. Commun.* **2020**, *11*, 5956. [CrossRef]
9. Zscheischler, J.; Westra, S.; van den Hurk, B.J.J.M.; Seneviratne, S.I.; Ward, P.J.; Pitman, A.; AghaKouchak, A.; Bresch, D.N.; Leonard, M.; Wahl, T.; et al. Future climate risk from compound events. *Nat. Clim. Chang.* **2018**, *8*, 469–477. [CrossRef]
10. Chopra, A.K.; Chakrabarti, P. The Koyna earthquake and the damage to Koyna Dam. *Bull. Seismol. Soc. Am.* **1973**, *63*, 381–397. [CrossRef]
11. Jansen, R. *Dams and Public Safety*; U.S. Department of the Interior, Bureau of Reclamation: Denver, CO, USA, 1980.
12. Xu, H.; Xu, Y.; Dai, H.; Li, D. Seismic performance of concrete gravity dams under combined reservoir water levels and ground motions. *Soil Dyn. Earthq. Eng.* **2019**, *116*, 538–552. [CrossRef]
13. Dasgupta, P.; Das, J.; Roy, S. Impact of climate change on flood frequency and intensity in the Indian subcontinent. *J. Hydrol.* **2020**, *590*, 125223.
14. Bathe, K.J. *Finite Element Procedures*; Prentice Hall: Upper Saddle River, NJ, USA, 2006.
15. Li, S. Coupled finite element–scaled boundary finite element method for transient analysis of dam–reservoir interaction. In *Computational Science and Its Applications—ICCSA 2011*; Murgante, B., Gervasi, O., Iglesias, A., Taniar, D., Apduhan, B., Eds.; Springer: Berlin/Heidelberg, Germany, 2011; pp. 26–34. [CrossRef]
16. Xu, H.; Xu, J.; Yan, D.; Chen, K.; Zou, D. An efficient dynamic coupling calculation method for dam–reservoir systems based on FEM. *Water* **2023**, *15*, 3095. [CrossRef]
17. Song, C.; Wolf, J.P. The scaled boundary finite-element method—Alias consistent infinitesimal finite-element cell method—For elastodynamics. *Comput. Methods Appl. Mech. Eng.* **1997**, *147*, 329–355. [CrossRef]
18. Zhao, L.H. Seismic Response Analysis of Arch Dams with Transverse Joints Considering Dam-Reservoir-Foundation Interaction. Ph.D. Thesis, Hohai University, Nanjing, China, 2006.
19. Yaseri, A.; Konrad, J.-M. Computation of amplification functions of earth dam–flexible canyon systems by the hybrid FEM–SBFEM technique. *Earthq. Eng. Struct. Dyn.* **2021**, *50*, 2883–2902. [CrossRef]
20. Wang, J.; Song, C. Scaled boundary finite element analysis of dam-reservoir interaction in layered half-space. *Soil Dyn. Earthq. Eng.* **2020**, *135*, 106189. [CrossRef]
21. Hallegatte, S.; Green, C.; Nicholls, R.J.; Corfee-Morlot, J. Future flood losses in major coastal cities. *Nat. Clim. Chang.* **2013**, *3*, 802–806. [CrossRef]
22. UNDRR. *Global Assessment Report on Disaster Risk Reduction 2019*; United Nations Office for Disaster Risk Reduction: Geneva, Switzerland, 2019; Available online: https://gar.undrr.org/ (accessed on 30 June 2025).
23. IPCC. *Climate Change 2021: Impacts, Adaptation and Vulnerability*; Intergovernmental Panel on Climate Change: Geneva, Switzerland, 2021; Available online: https://www.ipcc.ch/report/ar6/wg2/ (accessed on 30 June 2025).
24. Zhang, L.; Liu, Y.; Song, C. A scaled boundary finite element method for dynamic analysis of dam-reservoir systems under earthquake excitation. *Eng. Struct.* **2019**, *197*, 109402. [CrossRef]
25. Chen, D.; Chen, K.; Zou, D. High-resolution numerical modeling of dam–reservoir–foundation systems using SBFEM. *J. Comput. Phys.* **2021**, *429*, 110018. [CrossRef]
26. Hariri-Ardebili, M.A.; Saouma, V.E. Seismic fragility analysis of concrete dams: A state-of-the-art review. *Eng. Struct.* **2016**, *128*, 374–399. [CrossRef]

27. Arheimer, B.; Lindström, G. Climate impact on floods: Changes in high flows in Sweden in the past and the future (1911–2100). *Hydrol. Earth Syst. Sci.* **2015**, *19*, 771–784. [CrossRef]
28. Blöschl, G.; Hall, J.; Viglione, A.; Perdigão, R.A.P.; Parajka, J.; Merz, B.; Lun, D.; Arheimer, B.; Aronica, G.T.; Bilibashi, A.; et al. Changing climate both increases and decreases European river floods. *Nature* **2019**, *573*, 108–111. [CrossRef] [PubMed]